JOURNAL OF AIRCRAFT
Vol. 32, No. 2, March–April 1995

Wing Flutter Boundary Prediction Using Unsteady Euler Aerodynamic Method

Elizabeth M. Lee-Rausch* and John T. Batina†
NASA Langley Research Center, Hampton, Virginia 23681

Modifications to an existing three-dimensional, implicit, upwind Euler/Reynolds-averaged Navier-Stokes code (CFL3D Version 2.1) for the aeroelastic analysis of wings are described. These modifications, which were previously added to CFL3D Version 1.0, include the incorporation of a deforming mesh algorithm and the addition of the structural equations of motion for their simultaneous time-integration with the governing flow equations. This article gives a brief description of these modifications and presents unsteady calculations that check the modifications to the code. Euler flutter results for an isolated 45-deg swept-back wing are compared with experimental data for seven freestream Mach numbers that define the flutter boundary over a range of Mach number from 0.499 to 1.14. These comparisons show good agreement in flutter characteristics for freestream Mach numbers below unity. For freestream Mach numbers above unity, the computed aeroelastic results predict a premature rise in the flutter boundary as compared with the experimental boundary. Steady and unsteady contours of surface Mach number and pressure are included to illustrate the basic flow characteristics of the time-marching flutter calculations and to aid in identifying possible causes for the premature rise in the computational flutter boundary.

Nomenclature

A_{ij} = generalized aerodynamic force resulting from pressure induced by mode j acting through mode i
b = root semichord
C_p = pressure coefficient
c = root chord
c_i = generalized damping of mode i
k = reduced frequency, $(\omega c/2U_\infty)$
k_i = generalized stiffness of mode i
M_∞ = freestream Mach number
$\hat{m}$ = measured wing panel mass
m_i = generalized mass of mode i
Q_i = generalized aerodynamic force computed by integrating the pressure weighted by the structural mode i
q_i = generalized displacement of mode i
T = dimensional time
U_F = flutter speed
U_∞ = streamwise freestream speed
$\boldsymbol{u}_i$ = load vector
v = volume of a truncated cone having streamwise root chord as lower base diameter, streamwise tip as upper base diameter, and panel span as height
$\boldsymbol{x}_i$ = state vector
α = steady-state angle of attack
Θ = integral of the state-transition matrix
μ = mass ratio, $(\hat{m}/\rho v)$
σ_j = damping associated with mode j of the aeroelastic response
Φ = state-transition matrix
ω = angular frequency
ω_j = frequency associated with mode j of the aeroelastic response
ω_α = uncoupled natural frequency of the wing first torsion mode

Received Feb. 25, 1993; presented as Paper 93-1422 at the AIAA/ASME/ASCE/AHS/ASC 34th Structures, Structural Dynamics, and Materials Conference, La Jolla, CA, April 19–21, 1993; revision received May 2, 1994; accepted for publication May 17, 1994.

*Research Engineer, Aeroelastic Analysis and Optimization Branch, Structural Dynamics Division. Member AIAA.

†Senior Research Engineer, Aeroelastic Analysis and Optimization Branch, Structural Dynamics Division. Associate Fellow AIAA.

Introduction

RESEARCH during the last decade on the application of computational fluid dynamics (CFD) methods to unsteady flows and aeroelastic analysis has been rapidly progressing. Edwards and Malone[1] recently presented a survey on the status of computational methods for unsteady aerodynamic and aeroelastic analysis with an emphasis on methods for transonic flows. The transonic speed range has been a main focus of activity because flutter dynamic pressures are typically critical (lower) in this speed range. Much of this research, especially for three-dimensional configurations, has focused on the development of finite difference methods for the solution of the transonic small disturbance (TSD) and full potential (FP) equations.[1] One reason for the focus on the FP and TSD methods is that the reduced memory and run-time requirements of these methods in comparison with the higher-order methods have made them more viable for use in aeroelastic analyses of three-dimensional configurations. Edwards and Malone[1] reported on 13 aeroelastic studies of flexible wings and flexible wings/rigid body configurations that utilized the TSD and FP methods. These studies, which compare flutter boundary calculations with experimental data, provide important applications of these CFD methods.

Reference 1 points out that many critical challenges facing computational aeroelasticity will require the modeling of increasingly more complex flow physics. To meet these challenges, researchers have begun to develop higher-order methods involving the Euler and Navier-Stokes equations for unsteady aerodynamic and aeroelastic analysis. With recent advances in algorithm development and computer hardware, higher-order methods utilizing the Euler and Navier-Stokes equations have been used in three-dimensional aeroelastic applications[2–11]; however, the number of these applications lags behind those utilizing the TSD and FP methods, largely in part because of their increased computational requirements.

The research described in Refs. 2–11 represents important steps in the development of three-dimensional Euler and Navier-Stokes methods for aeroelastic analysis. However, continuing studies are needed to validate these methods for the prediction of aeroelastic response and flutter. Robinson et al.[3] performed time-marching flutter calculations for an isolated 45-deg swept-back wing using an Euler code. A novel aspect of the capability described in Ref. 3 was the deforming mesh algorithm that was used to move the mesh so that it conformed continuously to the instantaneous position of the wing. The results presented compared favorably with the experimental data and with results from a transonic small disturbance code for the single flutter point analyzed.

The purpose of the present work is to further demonstrate and assess the capability presented in Ref. 3 by completing the flutter boundary for the simple, well-defined, isolated 45-deg swept-back wing configuration using the Euler equations. The wing analyzed in these studies is the first AGARD standard aeroelastic configuration for dynamic response, and its flutter data is an accepted set with which to test codes.[12] In Ref. 3, modifications were made to an existing three-dimensional, unsteady Euler/Reynolds-averaged Navier-Stokes code (CFL3D Version 1.0) for the aeroelastic analysis of wings. These modifications included the incorporation of a deforming mesh algorithm and the addition of the structural equations of motion for their simultaneous time-integration with the governing flow equations. The deforming mesh algorithm and the structural equations of motion described in Ref. 3 have been added to the most recently released version of CFL3D, Version 2.1, by the present authors. This article gives a brief description of these modifications and presents unsteady calculations that check the modifications to the code. Results from calculations performed for a rigid wing undergoing forced pitching and plunging motions are presented to test the performance of the deforming mesh algorithm. Aeroelastic results for the 45-deg swept-back wing at a freestream Mach number of 0.9 are compared to those presented in Ref. 3 to check the addition to the structural equations of motion. Calculated flutter results for the same 45-deg swept-back wing are compared with the experimental data for seven freestream Mach numbers that define the flutter boundary over a range of Mach number from 0.499 to 1.14. Steady-state Mach contours of the initial flowfields are also included in the discussion of the aeroelastic results to illustrate the basic flow characteristics of the time-marching flutter calculations at selected freestream Mach numbers. Instantaneous surface pressure contours during an aeroelastic transient at $M_\infty = 0.99$ are presented to demonstrate changes in the flowfield that are induced by the aeroelastic motions.

Upwind Euler/Reynolds-Averaged Navier-Stokes Algorithm

The time-dependent Euler equations are solved within the CFL3D[13,14] code by a three-factor, implicit, finite volume algorithm based on upwind-biased spatial differencing. The algorithm, which is a cell-centered scheme, uses upwind differencing based on either flux-vector splitting or flux-difference splitting. Both types of upwind differencing account for the local wave-propagation characteristics of the flow and sharply capture shock waves. Also, because these schemes are naturally dissipative, additional artificial dissipation terms are not necessary. Several types of flux-limiting are available within the code to prevent oscillations in the solution near shock waves. These oscillations are typically found in results from higher-order schemes. For unsteady cases, the original algorithm contains the necessary metric terms for a rigidly translating and rotating mesh that moves without deforming. For cases involving a deforming mesh, however, an additional term accounting for the change in cell volume must be included in the time-discretization of the governing equations. This modification is implemented as described in Ref. 3. The aeroelastic equations of motion were implemented in the more recent Version 2.1. In addition to other improvements, this more recent version of the code contains several options for computing multiblock solutions that will be utilized in future computations.

Deforming Mesh Algorithm

In the time-marching aeroelastic calculations, the mesh must be updated at every time level so that it conforms to the aeroelastically deformed shape of the wing. Because the aeroelastic motion of the wing may be general in nature and is not known a priori, a general mesh updating procedure is necessary. One such method, the deforming mesh algorithm, models the mesh as a network of springs and solves the static equilibrium equations for this network to determine the new locations of the mesh grid points. This algorithm was originally developed by Batina[15] for tetrahedral cells and extended by Robinson et al.[3] for hexahedral cells. The edge of each hexahedral cell is modeled as a spring whose stiffness is inversely proportional to the length of the edge raised to a power. In order to control cell shearing and to prevent the collapse of the cell, diagonal springs are added along the faces of each cell. Similarly, the stiffness of the diagonal springs is also inversely proportional to the length of the diagonal raised to a power. As suggested in Ref. 3, a power of three was used in the present calculations.

At each time level, the grid points on the outer boundary are held fixed, and the displacement of the wing surface is specified. For aeroelastic calculations, the displacement is determined from the integration of the structural equations of motions. The new locations of the interior grid points are then determined by solving the static equilibrium equations that result from a summation of forces in the x-, y-, and z-coordinate directions at each grid point. These static equilibrium equations are solved using a predictor-corrector method. The new grid point locations are first predicted by an extrapolation from the previous two time levels and then corrected by using several Jacobi iterations of the static equilibrium equations. In the present calculations four Jacobi iterations are sufficient to move the mesh.

Time-Marching Aeroelastic Analysis

The time-marching aeroelastic procedure used in this study is typical of those currently in use.[3,11,16] In general, the equations are solved by assuming that the general motion of the wing can be described by a separation of time and space variables in a finite modal series. This modal series consists of the summation of the free vibration modes weighted by the generalized displacements. After applying Lagrange's equations to this system, the aeroelastic equations of motion can then be written for each vibration mode i as

$$m_i\ddot{q}_i + c_i\dot{q}_i + k_iq_i = Q_i \tag{1}$$

The superscript dots in Eq. (1) represent differentiation with respect to time. The fluid forces as determined by the CFD code are coupled with the structural equations of motion through the generalized aerodynamic forces.

The solution procedure implemented in this study for integrating Eq. (1) in time is that described by Edwards et al.[17,18] Equation (1) is written as a linear state equation such that

$$\dot{\boldsymbol{x}}_i = A\boldsymbol{x}_i + B\boldsymbol{u}_i \tag{2}$$

where A and B are coefficient matrices that result from the change of variables $\boldsymbol{x}_i = [q_i\dot{q}_i]^T$, and $\boldsymbol{u}_i$ is the nondimensional representation of the generalized force Q_i. Equation (2) is integrated in time using a modified state-transition matrix structural integrator[17] implemented as a predictor-corrector procedure. The prediction for $\boldsymbol{x}_i^{n+1}$, $\tilde{\boldsymbol{x}}_i^{n+1}$, is given by

$$\tilde{\boldsymbol{x}}_i^{n+1} = \Phi\boldsymbol{x}_i^n + \Theta B(3\boldsymbol{u}_i^n - \boldsymbol{u}_i^{n-1})/2 \tag{3}$$

where Φ is the state-transition matrix, and Θ is the integral of the state-transition matrix from time step n to $n + 1$. The predicted value of the generalized displacement $\tilde{x}_i^{n+1}$ is used to update the mesh for the next flowfield calculation, which is used in turn to evaluate the nondimensional generalized force $\tilde{u}_i^{n+1}$. These values are then used in the corrector step to determine x_i^{n+1}, given by

$$x_i^{n+1} = \Phi x_i^n + \Theta B(\tilde{u}_i^{n+1} + u_i^n)/2 \tag{4}$$

In a time-marching aeroelastic analysis, the calculation of each flutter point is begun by obtaining a static aeroelastic solution about the wing. In this study, a steady-state solution is first computed about the rigid wing. The next step is to allow the wing to deform to the steady loads until a static aeroelastic solution is obtained. The calculation of the static deformation is obtained using the aeroelastic equations of motion. For this time-marching calculation, however, the structural damping ratio of the wing is set to a number such that the dynamic system is near critically damped. The aeroelastic equations of motion are then marched simultaneously in time with the governing flow equations until the wing no longer deforms under the aerodynamic loads. When the system is near critically damped, this calculation requires less computational time than if no damping were added. The static aeroelastic solution is then used as the starting point for the time-marching dynamic aeroelastic solution. Since the wing analyzed in the present work has a symmetric airfoil section, at zero degree angle of attack this configuration will have no static deflection. Therefore, for this wing, the steady, rigid solutions could be used as the starting solutions for the aeroelastic time-marching calculations.

In order to bracket the flutter point, the static aeroelastic and dynamic aeroelastic computations are computed at several values of dynamic pressure (typically three values), which ranged from 80 to 120% of the experimental values, depending on the freestream Mach number. In each of the dynamic aeroelastic calculations, the motion of the wing is initiated by specifying a small initial velocity for the first two modes. The resulting transients are analyzed for their damping and frequency content with the modal identification technique of Bennett and Desmarais.[19] The computed flutter dynamic pressure can then be determined after interpolating the specified dynamic pressures as a function of damping for the dominant mode at flutter. The flutter frequency is obtained in the same manner.

Pulse Transfer-Function Analysis

Generalized aerodynamics forces (GAFs) can be obtained by calculating several cycles of a forced harmonic oscillation and using the last cycle of oscillation to determine the load. This requires one time-marching calculation for each value of reduced frequency and each mode of interest. In contrast, the GAFs may be determined for a wide range of reduced frequency in a single time-marching calculation for each mode using the pulse transfer-function analysis. In the pulse analysis, the unsteady force is computed indirectly from the response of the flowfield due to a wing motion that is represented by a smoothly varying, exponentially shaped pulse. A fast Fourier transform of the unsteady force is divided by the Fourier transform of the displacement to obtain the GAF. The pulse transfer-function analysis has been previously employed to determine the GAFs, which are used in aeroelastic analyses.[3,16,20-22] Results presented in Refs. 3, 16, and 20–22 have shown that the analysis is valid for predicting the small perturbation response about a nonlinear flowfield.

Wind-Tunnel Model Description

The wing being analyzed in this study is the first AGARD standard aeroelastic configuration for dynamic response, Wing 445.6,[12] which was tested in the Transonic Dynamics Tunnel (TDT) at NASA Langley Research Center.[23] The Wing 445.6 has a quarter-chord sweep angle of 45 deg, a panel aspect ratio of 1.65, a taper ratio of 0.66, and a NACA 65A004 airfoil section. A planform view of this wing is shown in Fig. 1. Several different models of the Wing 445.6 were tested in the TDT, including both full span and semispan models. The model used in this study was one of the semispan wind-tunnel-wall-mounted models that was constructed of laminated mahogany. In order to obtain flutter data for a wide range of Mach number and density conditions in the TDT, holes were drilled through several of the mahogany wings to reduce their stiffness. The aerodynamic shape of the original wing was preserved by filling the holes with rigid foam plastic. The model designated as "WEAK3" in Ref. 23 is analyzed herein. The flutter data for this model tested in air is reported in Ref. 23 over a range of Mach number from 0.499 to 1.141.

The Wing 445.6 is modeled structurally using the first four natural vibration modes that are illustrated in Fig. 2. Figure 2 shows the deflection contours associated with the natural modes. These modes that are numbered 1–4 represent first bending, first torsion, second bending, and second torsion, respectively, as calculated by a finite element analysis.[23] The modes have natural frequencies that range from 9.6 Hz for the first bending mode to 91.54 Hz for the second torsion mode. As suggested in Ref. 23, the experimentally determined modal frequencies were used in the time-marching flutter analysis. For the cases considered in this study, no structural damping is included in the aeroelastic equations of motion ($c_i = 0$ for all modes).

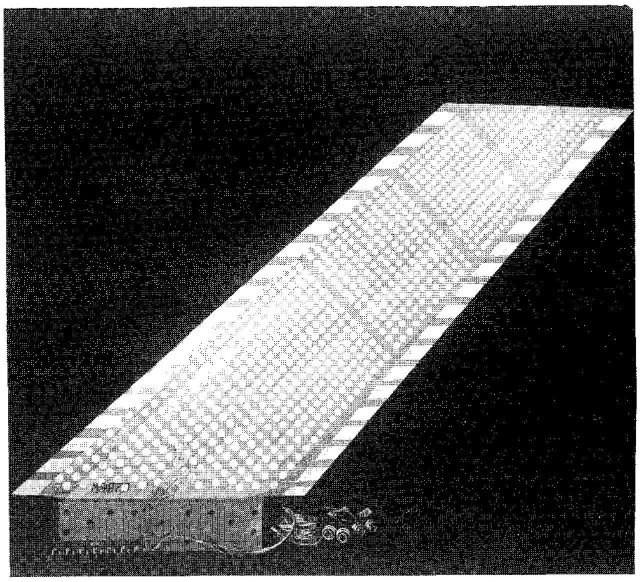

Fig. 1 Planform view of Wing 445.6.

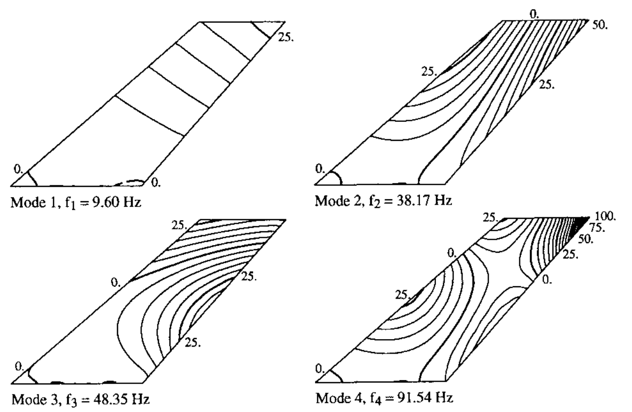

Fig. 2 Deflection contours of the natural vibrations modes for Wing 445.6.

Results and Discussion

Results are presented in this section for calculations about the Wing 445.6. All of the computational results were obtained using a 193 × 33 × 41 C-H-type grid with 193 points wrapped around the wing and its wake (129 points on the wing surface), 41 points distributed from the wing root to the spanwise boundary (25 points on the wing surface), and 33 points distributed radially from the wing surface to the outer boundary. This mesh topoplogy was chosen rather than a C-O-type topology because the wind-tunnel model has a sheared-off tip. A partial view of the surface mesh on the wing and symmetry plane is shown in Fig. 3. Its outer boundaries extend 10 local chord lengths to the upstream and downstream boundaries, 10 local chord lengths to the upper and lower boundaries, and 1 semispan length off of the tip. Note that this grid is identical to the one used in Ref. 3. A steady-state grid resolution study at $M_\infty = 0.96$ and 1.141 indicated that at these higher Mach numbers further refinement of the grid is required in the spanwise direction to completely resolve the spanwise gradients. However, the 193 × 33 × 41 grid is sufficient to provide accurate aeroelastic results for all of the Mach numbers analyzed.

For all of the calculations, the Euler equations are solved using flux-vector splitting and a smooth flux-limiter. Convergence to steady state was accelerated using local time-stepping, mesh sequencing, and multigrid cycling. For time-marching calculations, the nondimensional global time-step (based on the root chord and the freestream speed of sound) was 0.05456. The in-core memory requirement for this grid was 25 MWords on a Cray-2 computer, which is 15.6 MWords over what is required for the unmodified CFL3D Version 2.1. Recent coding modifications have reduced the additional memory requirements for the aeroelastic version by approximately 50%, and so the current grid would now require 17.4 Mw. Each of the steady-state calculations required approximately 3–4 h of CPU time on a Cray-2 computer to converge the solution to an acceptable level (6 orders of magnitude). Aeroelastic transients were computed at each dynamic pressure for approximately 2 cycles of the lowest frequency modal motion. These calculations typically required 8 h of CPU time. Since aeroelastic transients were computed for three different values of dynamic pressure at each freestream Mach number, the total computational cost for each flutter point (including the steady-state solution) was approximately 28 h of CPU time.

Pulse Transfer-Function Results

The generalized forces for the Wing 445.6 at $M_\infty = 0.9$ were computed using the pulse transfer-function analysis method described in a preceding section. The pulse calculations were restarted from a steady-state flow condition at an angle of attack of $\alpha = 0$ deg. A plunging motion and a pitching motion about the root quarter-chord, which are defined as modes h and θ, respectively, were analyzed. These simple "modes" were chosen in order that the motion of the wing could be simulated not only by the deforming mesh algorithm, but also by a rigid translation and rotation of the grid. The maximum amplitude of the plunging motion was 0.01 root chord lengths, and the maximum pitch amplitude was 1 deg. The results of the pulse analyses, shown in Fig. 4, are plotted in terms of the real and imaginary components of the unsteady forces as a function of k, which is defined by $(\omega b/U_\infty)$. The generalized force A_{hh} is the lift due to plunge, $A_{h\theta}$ is the lift coefficient due to pitching, $A_{\theta h}$ is the pitching moment due to plunge, and $A_{\theta\theta}$ is the pitching moment due to pitch. As shown in Fig. 4, the forces from the pulse analysis obtained using the deforming mesh agree very well with the forces obtained using the rigidly moving mesh. This good agreement between the results verifies, for small motions, the three-dimensional deforming mesh capability that was implemented in the code.

Flutter Results

Flutter characteristics were determined for seven freestream Mach numbers, $M_\infty = 0.499, 0.678, 0.900, 0.960, 0.990, 1.072$, and 1.141, at $\alpha = 0$-deg angle of attack. Each time-marching calculation was restarted from the steady-state solution about the rigid wing, and the motion of the wing was initiated by specifying a small initial velocity for the first two modes. The resulting transients were analyzed for their damping and frequency content with the model identification technique that was previously described. The computed flutter dynamic pressure and frequency were determined by interpolating the specified dynamic pressures and the computed frequencies to the zero damping value of the flutter mode. The flutter mode for all freestream Mach numbers considered in this study was dominated by motion in the first bending

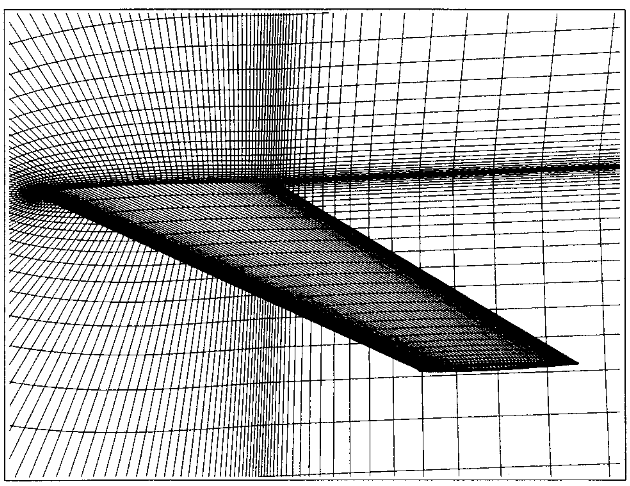

Fig. 3 Partial view of the 193 × 33 × 41 computational grid on the wing surface and symmetry plane.

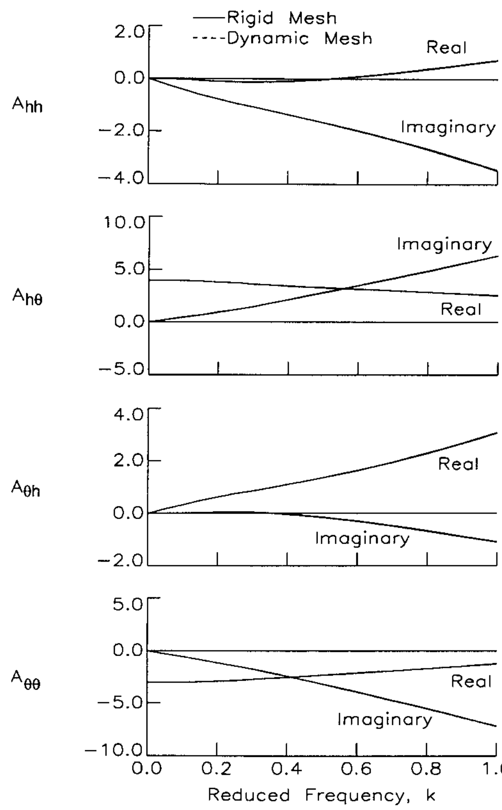

Fig. 4 Comparison of generalized aerodynamic forces for the rigid pitch and plunge of Wing 445.6 at $M_\infty = 0.9$ and $\alpha = 0$ deg.

mode. A summary of the computed flutter characteristics in terms of flutter speed index ($U_f/b\omega_\alpha\sqrt{\mu}$) and nondimensional flutter frequency ratio (ω/ω_α) is shown in Table 1. For M_∞ = 0.9, Ref. 3 reports a computed flutter speed index of 0.353 and a computed flutter frequency ratio of 0.42. These results agree very well with those shown in Table 1 for M_∞ = 0.9, which verifies the addition of the structural equations of motion to CFL3D version 2.1.

The computed flutter characteristics are compared with the experimentally measured values of flutter speed index and flutter frequency ratio in Fig. 5. The experimental data defines a typical transonic flutter "dip" with the bottom near M_∞ = 1.0. At the subsonic freestream Mach numbers (M_∞ = 0.499 and 0.678), the computed flutter speed indexes agree well with the experimental values, while the computed frequency ratios are slightly larger than the experimental values. It is interesting to note that at these subsonic freestream Mach numbers the computed flutter results are characterized by "hard" flutter crossings. In other words, small changes in dynamic pressure result in large changes in the damping of the flutter mode. At M_∞ = 0.9 and 0.96, the computed flutter speed indexes are less than the experimental values and the frequency ratios agree well with the experimental values. The computed flutter results at these freestream Mach numbers are characterized by a "mild" flutter crossing. Although there was no experimental flutter point determined at M_∞ = 0.99, computational results are included to aid in identifying the bottom of the flutter dip. The computational results at M_∞ = 0.99 are compared in Fig. 5 to estimated values of flutter speed and frequency determined from the faired curves in Fig. 16 of Ref. 23. These faired curves were based on the experimentally determined flutter points, the experimentally determined no-flutter track, and analytic calculations shown in Ref. 23 and are considered to be of reasonable accuracy.[24] The computational results at M_∞ = 0.99, as well as those at M_∞ = 1.072 and 1.141, indicate a premature rise in the computational flutter boundary as compared with the experimental boundary. Although the boundary is more sensitive to freestream Mach number in this range, the computed flutter results are still characterized by a mild flutter crossing.

Table 1 Summary of computed flutter results for Wing 445.6

M_∞	Flutter speed index	Flutter frequency ratio
0.499	0.439	0.597
0.678	0.417	0.539
0.900	0.352	0.425
0.960	0.275	0.343
0.990	0.310	0.373
1.072	0.466	0.541
1.141	0.660	0.764

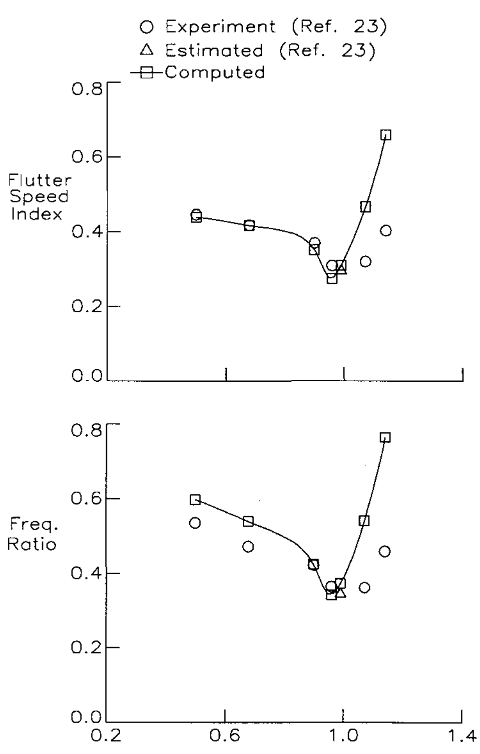

Fig. 5 Comparison of Euler flutter predictions with experimental data for Wing 445.6.

Computational results for this configuration obtained with linear theory and TSD methods were previously reported in Ref. 16. In Ref. 16, three sets of flutter results were presented: 1) results from a linear theory subsonic kernel-function program, 2) results using the linear potential equation and modeling the wing aerodynamically as a flat plate, and 3) results using the complete (nonlinear) TSD equation and including wing thickness. The flutter speed index and flutter frequency from the subsonic kernel-function and the potential equation compare well with the experimental data over the range of freestream Mach numbers from 0.338 to 1.141. (Note that the subsonic kernel-function results are limited to the subsonic freestream Mach numbers.) Results from the nonlinear TSD equation for the subsonic freestream Mach numbers 0.678, 0.901, 0.96 indicate that the flutter speed index is decreased by 1, 5, and 19%, respectively, from the experimental results with a similar decrease in the flutter frequency. These results are similar to the trend shown by the current computations in Fig. 5. Subsequent unpublished calculations by the authors of Ref. 16 indicate that flutter results for the supersonic freestream Mach numbers that were obtained with the nonlinear TSD equation are highly nonconservative. This trend is also consistent with the results shown in Fig. 5. It is counterintuitive that the higher-order methods utilizing the TSD and Euler equations should produce flutter results that compare less favorably with the experimental results than with the results based on linear methods. However, it is important to note that the modeling of the flow physics is incomplete even when using the TSD and Euler equations. The existence and effect of highly nonlinear flow phenomena such as strong shocks and viscous boundary layers must be investigated before any conclusions can be drawn.

Steady-state Mach contours of the initial flowfields on the upper wing surface are shown in Figs. 6a–6d to illustrate the basic flow characteristics at the selected freestream Mach numbers of 0.96, 0.99, 1.072, and 1.141, where time-marching flutter calculations were made. Mach contours for M_∞ = 0.499, 0.678, and 0.900, which are not shown, indicate a smooth expansion and recompression of the flow from the leading edge to the trailing edge, with very little variation in the spanwise direction and no supercritical flow. Mach contours shown in Fig. 6a indicate that at M_∞ = 0.96 an area of supercritical flow has formed on the wing. This area of supercritical flow does not terminate with a shock. Figure 6b shows that at M_∞ = 0.99 the areas of supercritical flow have expanded, and a normal shock has formed near the tip of the wing at approximately 25% of the local chord. Mach contours for M_∞ = 1.702 and 1.141, shown in Figs. 6c and 6d, respectively, indicate that with further increases in freestream Mach number, the normal shock transitions to an oblique shock located further downstream on the outboard portion of the wing at approximately 70% of the local chord. Also, at M_∞ = 1.141, the spanwise extent of the oblique shock has increased to approximately 50% of the outboard portion of the wing. Rapid changes in the steady-state flow conditions from M_∞ = 0.96 to 1.141 are indicated by the formation and move-

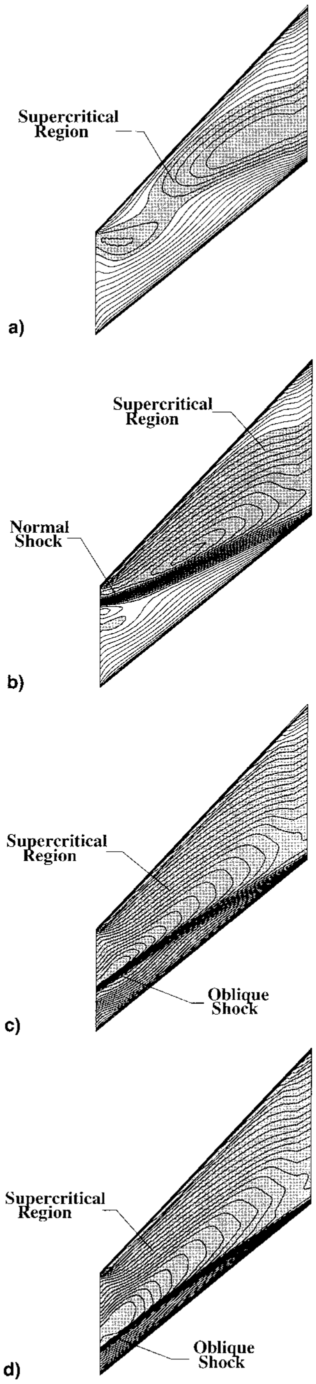

Fig. 6 Comparison of steady-state Mach contours on the upper surface of Wing 445.6. M_∞ = a) 0.96, b) 0.99, c) 1.072, and d) 1.141.

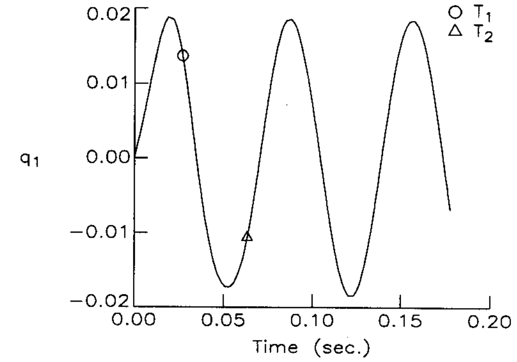

Fig. 7 Time history of the first generalized displacement for the Wing 445.6 at M_∞ = 0.99 and α = 0 deg.

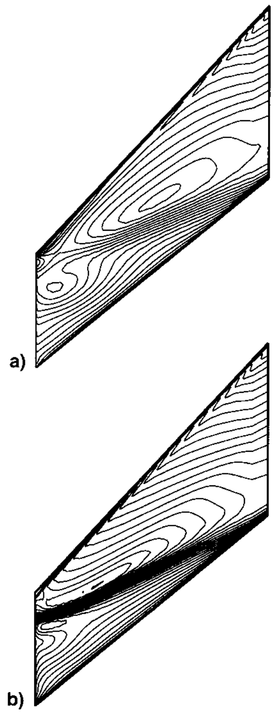

Fig. 8 Instantaneous surface contours of the pressure coefficient at time T_1 for the Wing 445.6 at M_∞ = 0.99 and α = 0 deg: a) upper and b) lower surfaces.

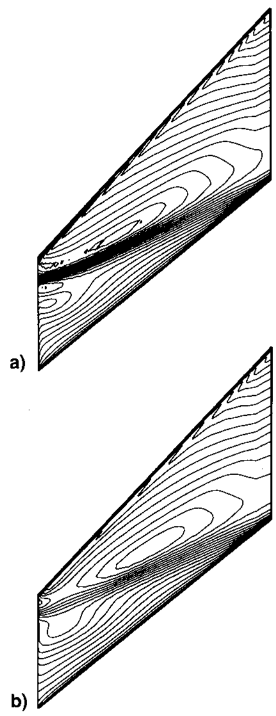

Fig. 9 Instantaneous surface contours of the pressure coefficient at time T_2 for the Wing 445.6 at M_∞ = 0.99 and α = 0 deg: a) upper and b) lower surfaces.

ment of a shock at the tip of the wing. This range of freestream Mach number also corresponds to the range of Mach numbers where the computed flutter boundary rapidly rises (see Fig. 5). Therefore, small variations due to errors associated with modeling deficiencies and computational deviations could be expected to have a large effect on the final flutter speed and frequency. Modeling deficiencies could be due to the neglect of the viscous effects. Computationally, these errors might be due to a lack of spatial convergence.

The rapid changes in the steady-state flowfield conditions from $M_\infty = 0.96$ to 1.141 suggest that, for a given freestream Mach number in this range, the flow characteristics can also change rapidly during an aeroelastic transient. Figure 7 shows the time history of the first generalized displacement q_1 for a time-marching aeroelastic transient at $M_\infty = 0.99$ and at a freestream dynamic pressure of 64.12 psf, which is 1.12 times the estimated experimental flutter dynamic pressure. Recall that q_1 corresponds to the first bending mode that is the dominant component of the flutter mode. The damping and frequency content of this aeroelastic trnsient indicates that the wing is dynamically unstable at this condition. Instantaneous surface contours of C_p are shown in Figs. 8 and 9 for the times T_1 and T_2, respectively, which are indicated in Fig. 7. Upper and lower surface pressures are shown at these points in time with $\Delta C_p = 0.02$. At T_1, contours on the upper surface indicate that an upper surface shock has disappeared, while contours on the lower surface indicate that a lower surface shock has strengthened and moved slightly downstream. Similarly, at T_2, the opposite has occurred. The shock has weakened on the lower surface and strengthened on the upper surface. Figures 8 and 9 therefore show that during the aeroelastic transient, rapid changes in surface pressures occur due to the formation and disappearance of a normal shock on the tip of the wing. Figures 8 and 9 also illustrate an unusual shock behavior during the aeroelastic transient in that there is little chordwise movement of the shock as it strengthens and weakens. For two-dimensional airfoils, significant shock weakening is usually accompanied by large shock motion.

Conclusions

Modifications to an existing three-dimensional, implicit, upwind Euler/Reynolds-averaged Navier-Stokes code (CFL3D Version 2.1) for the aeroelastic analysis of wings was described. These modifications included the incorporation of a deforming mesh algorithm and the addition of the structural equations of motion for their simultaneous time-integration with the governing flow equations. Euler results from calculations performed for a rigid wing undergoing forced pitching and plunging motions were presented to check the deforming mesh algorithm. Aeroelastic Euler results for a 45-deg swept-back wing at a freestream Mach number of 0.9 were compared to those presented in Ref. 3 to check the addition of the structural equations of motion. Calculated flutter results for the same 45-deg swept-back wing were compared with the experimental data for seven freestream Mach numbers that define the flutter boundary over a range of Mach number from 0.499 to 1.141. These comparisons showed good agreement in flutter characteristics for freestream Mach numbers below unity. For freestream Mach numbers above unity, the computed aeroelastic results predicted a premature rise in the flutter boundary as compared with the experimental boundary. Steady-state Mach contours of the initial flowfields illustrated rapid changes in the basic flow characteristics from $M_\infty = 0.96$ to 1.141, which is indicated by the formation and movement of a shock near the tip of the wing. Instantaneous surface pressure contours during an aeroelastic transient at $M_\infty = 0.99$ also demonstrated significant changes in the flowfield due to the formation and disappearance of a normal shock on the tip of the wing that is induced by the aeroelastic motions at this freestream Mach number.

Acknowledgments

The authors would like to thank Brian A. Robinson of McDonnell Aircraft Company, St. Louis, Missouri, for providing the computational grid and for sharing his experiences concerning the aeroelastic version of CFL3D. The authors would also like to thank James L. Thomas, W. Kyle Anderson, and Christopher L. Rumsey of the Computational Aerodynamics Branch, NASA Langley Research Center, and Sherrie L. Krist of ViGYAN Inc., Hampton, Virginia, for their many helpful discussions concerning CFL3D. Finally, the authors would like to thank their colleague, Robert M. Bennett, for sharing his many insights into computational aeroelasticity and flutter.

References

[1]Edwards, J. W., and Malone, J. B., "Current Status of Computational Methods for Unsteady Transonic Unsteady Aerodynamics and Aeroelastic Analysis," AGARD Structures and Materials Panel Specialist's Meeting on Transonic Unsteady Aerodynamics and Aeroelasticity, Paper 1, Oct. 1991.

[2]Guruswamy, G. P., "Time-Accurate Unsteady Aerodynamic and Aeroelastic Calculations of Wings Using Euler Equations," AIAA Paper 88-2281, April 1988.

[3]Robinson, B. A., Batina, J. T., and Yang, H. T. Y., "Aeroelastic Analysis of Wings Using the Euler Equations with a Deforming Mesh," *Journal of Aircraft*, Vol. 28, No. 6, 1991, pp. 778–788.

[4]Schuster, D., Vadyak, J., and Atta, E., "Static Aeroelastic Analysis of Fighter Aircraft Using a Three-Dimensional Navier-Stokes Algorithm," AIAA Paper 90-0435, Jan. 1990.

[5]Guruswamy, G. P., "Numerical Simulation of Vortical Flows on Flexible Wings," AIAA Paper 89-0537, Jan. 1989.

[6]Guruswamy, G. P., "Vortical Flow Computations on Swept Flexible Wings Using Navier-Stokes Equations," AIAA Paper 89-1183, April 1989.

[7]Guruswamy, G. P., "Navier-Stokes Computations on Swept-Tapered Wings, Including Flexibility," AIAA Paper 90-1152, April 1990.

[8]Guruswamy, G. P., "Vortical Flow Computations on a Flexible Blended Wing-Body Configuration," AIAA Paper 91-1013, April 1991.

[9]Obayashi, S., Guruswamy, G. P., and Goorjian, P., "Application of a Streamwise Upwind Algorithm for Unsteady Transonic Computations over Oscillating Wings," AIAA Paper 90-3103, Aug. 1990.

[10]Obayashi, S., and Guruswamy, G. P., "Unsteady Shock-Vortex Interaction on a Flexible Delta Wing," AIAA Paper 91-1109, April 1991.

[11]Rausch, R. D., Batina, J. T., and Yang, H. T. Y., "Three-Dimensional Time-Marching Aeroelastic Analyses Using an Unstructured-Grid Euler Method," AIAA Paper 92-2506, April 1992.

[12]Yates, E. C., Jr., "AGARD Standard Aeroelastic Configuration for Dynamic Response, Candidate Configuration I.-Wing 445.6," NASA TM 100492, Aug. 1987.

[13]Anderson, W. K., Thomas, J. L., and Van Leer, B., "Comparison of Finite Volume Flux Vector Splitting for the Euler Equations," *AIAA Journal*, Vol. 24, No. 9, 1986, pp. 1453–1460.

[14]Anderson, W. K., Thomas, J. L., and Rumsey, C. L., "Extension and Applications of Flux-Vector Splitting to Unsteady Calculations on Dynamic Meshes," AIAA Paper 87-1152, June 1987.

[15]Batina, J. T., "Unsteady Euler Algorithm with Unstructured Dynamic Mesh for Complex-Aircraft Aeroelastic Analysis," AIAA Paper 89-1189, April 1989.

[16]Cunningham, H. J., Batina, J. T., and Bennett, R. M., "Modern Wing Flutter Analysis by Computational Fluid Dynamics Methods," *Journal of Aircraft*, Vol. 25, No. 10, 1988, pp. 962–968.

[17]Edwards, J. W., Bennett, R. M., Whitlow, W., Jr., and Seidel, D. A., "Time-Marching Transonic Flutter Solutions Including Angle-of-Attack Effects," AIAA Paper 82-0685, May 1982.

[18]Edwards, J. W., Bennett, R. M., Whitlow, W., Jr., and Seidel, D. A., "Time-Marching Transonic Flutter Solutions Including Angle-of-Attack Effects," *Journal of Aircraft*, Vol. 20, No. 11, 1984, pp. 899–906.

[19]Bennett, R. M., and Desmarais, R. N., "Curve Fitting of Aeroelastic Transient Response Data with Exponential Functions," Flutter Testing Techniques NASA SP-415, May 1975.

[20]Seidel, D. A., Bennett, R. M., and Whitlow, W. W., "An Exploratory Study of Finite Difference Grids for Transonic Unsteady Aerodynamics," AIAA Paper 83-0503, Jan. 1983.

[21]Seidel, D. A., Bennett, R. M., and Ricketts, R. H., "Some Recent Applications of XTRAN3S," AIAA Paper 83-1811, July 1983.

[22]Rausch, R. D., Batina, J. T., and Yang, H. T. Y., "Euler Flutter Analysis of Airfoils Using Unstructured Dynamic Meshes," *Journal of Aircraft*, Vol. 27, No. 5, 1990, pp. 436–443.

[23]Yates, E. C., Jr., Land, N. S., and Foughner, J. T., Jr., "Measured and Calculated Subsonic and Transonic Flutter Characteristics of a 45 Deg Sweptback Wing Planform in Air and in Freon-12 in the Langley Transonic Dynamics Tunnel," NASA TN D-1616, March 1963.

[24]Yates, E. C., Jr., private communication, Hampton, VA, July 1992.